

# Total body CD4<sup>+</sup> T cell dynamics in treated and untreated SIV infection revealed by in vivo imaging

Michele Di Mascio,<sup>1</sup> Sharat Srinivasula,<sup>2</sup> Insook Kim,<sup>3</sup> Gorka Duralde,<sup>1</sup> Alexis St. Claire,<sup>1</sup> Paula DeGrange,<sup>4</sup> Marisa St. Claire,<sup>1</sup> Keith A. Reimann,<sup>5</sup> Erin E. Gabriel,<sup>1</sup> Jorge Carrasquillo,<sup>6</sup> Richard C. Reba,<sup>7</sup> Chang Paik,<sup>8</sup> and Henry C. Lane<sup>9</sup>

<sup>1</sup>AIDS Imaging Research Section, Division of Clinical Research, NIAID, NIH, Bethesda, Maryland, USA. <sup>2</sup>Clinical Research Directorate/Clinical Monitoring Research Program, Leidos Biomedical Research Inc., NCI Campus at Frederick, Frederick, Maryland, USA. <sup>3</sup>Applied/Developmental Research Directorate, Leidos Biomedical Research Inc., NCI Campus at Frederick, Frederick, Maryland, USA. <sup>4</sup>Battelle/Charles River-Integrated Research Facility, NIAID Frederick, Frederick, Maryland, USA. <sup>5</sup>MassBiologics, University of Massachusetts Medical School, Boston, Massachusetts, USA. <sup>6</sup>Molecular Imaging and Therapy Service, Radiology Department, Memorial Sloan Kettering Cancer Center, New York, USA. <sup>7</sup>Center for Infectious Disease Imaging, Radiology and Imaging Sciences, Clinical Center NIH, Bethesda, Maryland, USA. <sup>8</sup>Radiopharmaceutical Laboratory, Nuclear Medicine, Radiology and Imaging Sciences, Clinical Center, NIH, Bethesda, Maryland, USA. <sup>9</sup>Laboratory of Immunoregulation, Division of Intramural Research, NIAID, NIH, Bethesda, Maryland, USA.

The peripheral blood represents only a small fraction of the total number of lymphocytes in the body. To develop a more thorough understanding of T cell dynamics, including the effects of SIV/SHIV/HIV infection on immune cell depletion and immune reconstitution following combination antiretroviral therapy (cART), one needs to utilize approaches that allow direct visualization of lymphoid tissues. In the present study, noninvasive in vivo imaging of the CD4<sup>+</sup> T cell pool has revealed that the timing of the CD4<sup>+</sup> T cell pool reconstitution following initiation of ART in SIV-infected nonhuman primates (NHPs) appears seemingly stochastic among clusters of lymph nodes within the same host. At 4 weeks following initiation or interruption of cART, the changes observed in peripheral blood (PB) are primarily related to changes in the whole-body CD4 pool rather than changes in lymphocyte trafficking. Lymph node CD4 pools in long-term antiretroviral-treated and plasma viral load-suppressed hosts appear suboptimally reconstituted compared with healthy controls, while splenic CD4 pools appear similar between the 2 groups.

## Introduction

In previous work (1), we have demonstrated the feasibility of in vivo imaging of the whole-body CD4 pool of simian/human immunodeficiency virus-infected (SHIV-infected) nonhuman primates (NHPs) using a radiolabeled humanized nondepleting anti-CD4 mAb (hu-IgG4/OKT4A) and single-photon emission CT (SPECT). Strong correlations ( $\rho > 0.75$ ) were noted between radiotracer uptake in spleen, tonsil and axillary lymph nodes (LNs), and peripheral blood (PB) CD4<sup>+</sup> T cell counts. Minimal uptake was noted in the gastrointestinal tract. These data highlighted the limitations of using the PB CD4<sup>+</sup> T cell counts to infer the level of whole-body immunocompetence and challenged the prevalent notion that the gut is the major reservoir of CD4<sup>+</sup> T cells in the body. It has been suggested that the increases in the numbers of CD4<sup>+</sup> T cells in the PB of HIV-1-infected subjects after initiation of combination antiretroviral therapy (cART) result from a combination of 2 phenomena: decreases in immune activation leading to an increase in distribution of cells from lymphoid tissues (LTs) to PB, and increases in the total number of CD4 cells in the body due to a decrease in cell death (2). Determination of the relative contributions of these 2 components requires simultaneous and repeated measurements of both PB and total LTs. This is now possible through the use of PB sampling and noninvasive, total body imaging with CD4-specific probes. Initial longitudinal imaging studies to examine the effects of cART were compromised due to the immunogenicity of the probe (1). Accordingly, the probes were modified from intact antibodies into F(ab')<sub>2</sub> fragments that were then coupled with the  $\gamma$  emitter <sup>99m</sup>Technetium (<sup>99m</sup>Tc) without loss in binding

**Conflict of interest:** The authors have declared that no conflict of interest exists.

**Submitted:** October 31, 2017

**Accepted:** May 29, 2018

**Published:** July 12, 2018

**Reference information:**

JCI Insight. 2018;3(13):e97880.

<https://doi.org/10.1172/jci.insight.97880>.

insight.97880.

**Table 1. Spearman rank correlation between peripheral blood CD4<sup>+</sup> T cell count and organ radiotracer uptake**

	F(ab') <sub>2</sub> -OKT4A (n = 11)		F(ab') <sub>2</sub> -CD4R1 (n = 19)	
	Spearman rank correlation	P value	Spearman rank correlation	P value
Spleen	0.7	<0.01	0.76	<0.01
Axillary LNs	0.71	<0.01	0.55	<0.01
Submandibular LNs	0.61	0.02	0.52	0.01
Inguinal LNs	0.49	0.06	0.61	<0.01
Heart	0.45	0.08	0.21	0.19
Kidney	0.44	0.09	0.32	0.09
Bone marrow	-0.25	0.77	0.11	0.33
Thymus	0.49	0.06	0.15	0.27
Plasma SUV	0.11	0.37	0.11	0.32

Spearman rank correlation between peripheral blood CD4<sup>+</sup> T cell count and organ radiotracer uptake (radiotracer retention). The retention of radiotracer for each VOI was obtained from the maximum activity in the VOI normalized on the maximum activity in the liver.

affinity to CD4 receptors. Utilizing F(ab')<sub>2</sub> fragments of the humanized CDR-OKT4A/huIgG4 and of the rhesus recombinant CD4R1-OKT4A/rhIgG1 mAbs, hereafter called F(ab')<sub>2</sub>-OKT4A and F(ab')<sub>2</sub>-CD4R1, respectively, longitudinal studies became possible, as recently demonstrated by our group in the settings of hematopoietic stem cell transplantation following total body irradiation in NHPs (3). These modified radiotracers produced images with lower background compared with the intact mAb and considerably less immunogenicity than the intact antibodies. The current work examines longitudinal changes in the CD4 pool in SIV-infected NHPs following the initiation or interruption of cART.

## Results

The in vitro and ex vivo specificity tests and the in vivo stability and biodistribution studies were performed for both the <sup>99m</sup>Tc-F(ab')<sub>2</sub>-OKT4A, and the <sup>99m</sup>Tc-F(ab')<sub>2</sub>-CD4R1 radiotracers, as previously described (1, 3). These preliminary studies showed high immunoreactivity and optimal stability of both probes, as reported in Supplemental Figure 1 (supplemental material available online with this article; <https://doi.org/10.1172/jci.insight.97880DS1>).

*Relationships between LTs and PB CD4 pools in SIV-infected NHPs.* A summary of the imaging experiments and characterizations of the monkeys imaged are shown in Supplemental Table 1. Eleven NHPs, spanning a range of CD4<sup>+</sup> T cell counts from 28–1,324, received 6.04 ± 1.27 mCi of <sup>99m</sup>Tc-F(ab')<sub>2</sub>-OKT4A, and 19 NHPs, spanning a range of CD4<sup>+</sup> T cell counts from 7–1,718 cells/μl, received 6.12 ± 1.07 mCi of <sup>99m</sup>Tc-F(ab')<sub>2</sub>-CD4R1 i.v. after fasting for at least 8 hours. No association was found between the mean fluorescence intensity (MFI) of CD4 cells in the PB and the PB CD4<sup>+</sup> T cell count (not shown). Therefore, any differences in probe binding likely reflected differences in total numbers of cells rather than differences in the number of antibody molecules bound per cell. Whole-body SPECT images were acquired from the top of the skull to the inguinal region for all animals at 4–6 hours after radiotracer injection (p.r.i.) and, for a subgroup of animals, also at 19 hours p.r.i. The semi-quantitative analyses of the 3D-SPECT images are here summarized for all the images acquired at 4–6 hours p.r.i. Whole-body region of interest (ROI) analyses revealed no significant correlations between PB CD4<sup>+</sup> T cell count and hepatic uptake (OKT4A:  $\rho = -0.04$ ,  $P = 0.46$ ,  $n = 11$ ; CD4R1:  $\rho = -0.21$ ,  $P = 0.20$ ,  $n = 19$ ). In contrast, strong correlations were found between the radiotracer retention in LTs and PB CD4<sup>+</sup> T cell count (Table 1 and Figure 1). The highest Spearman rank correlations were noted for the spleen ( $\rho > 0.70$ ,  $P < 0.01$ ), followed by the axillary and submandibular LNs ( $\rho > 0.52$ ,  $P < 0.05$ ), suggesting that the majority of the radiotracer uptake in these organs is the result of specific binding of the radiotracer to CD4<sup>+</sup> cells. Moreover, nonstatistically significant associations were observed between radiotracer uptake in kidney, heart, thymus, and bone marrow (proximal and central humerus) and PB CD4<sup>+</sup> T cell count, suggesting that the majority of the radiotracer uptake in those organs was the result of nonspecific uptake. This pattern of correlations, or lack thereof, was also observed with the SUV<sub>max</sub> and, overall, were found to be remarkably similar to those reported for the parent radiotracer <sup>111</sup>In-DTPA-CDR-OKT4A/huIgG4 (1). Moreover, similar to what was observed with the intact anti-CD4 mAb, the SPECT imaging or direct radioactivity measurements of any

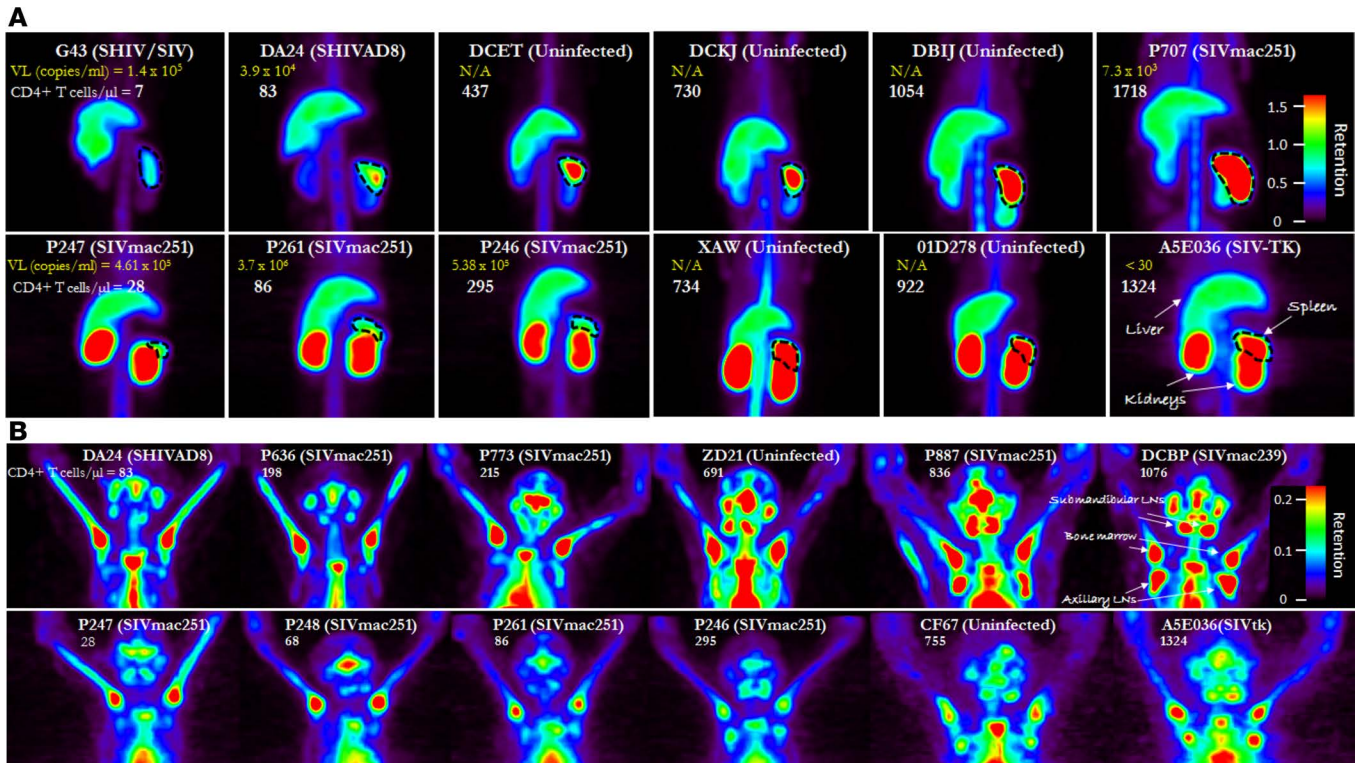


**Figure 1. Cross-sectional comparison of LTs uptakes.** Maximum intensity projection–single-photon emission CT (MIP-SPECT) images in the abdominal (**A**) or skull (**B**) field of view (FOV) in monkeys characterized by different peripheral blood CD4 cell counts. Top panels: animals were imaged with  $^{99m}\text{Tc}-(\text{ab}')_2\text{-CD4R1}$ . Bottom panels: animals were imaged with  $^{99m}\text{Tc}-\text{F}(\text{ab}')_2\text{-OKT4A}$ . All images are adjusted between monkeys on the maximum liver uptake. Tissue uptakes were converted to rainbow color scale as shown in the color bar, where red indicates highest retention.

subcompartment (jejunum, ileum, and ascending and descending colon) of the small and large intestine did not reveal differences between animals with high and low CD4<sup>+</sup> T cell counts (see below and Supplemental Figures 2 and 5), with the overall uptake in these ROI close to background levels, consistent with the low density of lymphocytes per unit mass of these organs. Similar distributions of the tracer, but with less contrast, were observed from the images acquired at 19 hours p.r.i.

The 30 (12 uninfected and 18 SIV/SHIV-infected) rhesus macaques imaged in this study received a total of 59 SPECT imaging studies (Supplemental Table 2). A repeated measurements univariate analysis of all animals revealed that PB CD4<sup>+</sup> T cell count was statistically significantly associated with the size of the splenic CD4 pool and (in SIV-infected animals) the plasma viral load (both  $P < 0.001$ ). The PB CD4<sup>+</sup> T cell count was also univariately associated with the size of the CD4 pool of the axillary, inguinal, and submandibular LNs in all animals (all  $P < 0.01$ ). The size of the submandibular pool was also associated with the plasma viral load in infected animals ( $P = 0.046$ ). In a multivariate analysis among the infected animals, adjusting for the PB CD4<sup>+</sup> T cell count, only the size of the splenic CD4 pool remained associated with the plasma viral load ( $P = 0.01$ ). For animals with similar PB CD4<sup>+</sup> T cell counts, a 1-log increase in plasma viremia was associated with approximately an 8% depletion of the splenic CD4 pool.

Similar to what was observed with the intact mAb (1), the relationship between the CD4<sup>+</sup> T cell count in the PB and the retention (or uptake) of radiotracer in LTs appeared to be nonlinear (Supplemental Figure 3), suggesting that smaller changes in tissue CD4 pools are expected at higher levels of PB CD4<sup>+</sup> T cell counts.

Among the 30 animals imaged in this study, 11 healthy uninfected animals (with PB CD4<sup>+</sup> T cell count  $>600$  cells/ $\mu\text{l}$ ) were imaged at baseline; 10 animals with advanced SIV or SHIV infection (CD4<sup>+</sup> T cell count  $<300$  cells/ $\mu\text{l}$ ) were imaged during the chronic phase of infection ( $> 5$  months from viral inoculation); and 6 animals with SIV infection were imaged after being treated with cART for more than 5 months (plasma SIV RNA levels  $<30$  copies/ml in 5 animals and 950 copies/ml in the other). Compared with healthy uninfected controls ( $n = 11$ , mean PB CD4<sup>+</sup> T cell count 962 cells/ $\mu\text{l}$ , 95% CI, 773–1,151 cells/ $\mu\text{l}$ ), long-term

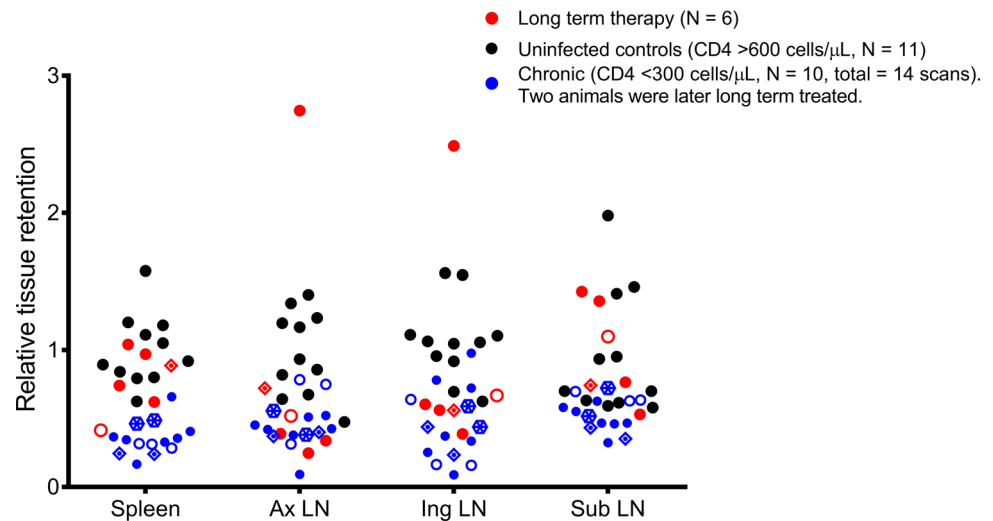


**Figure 2. Comparison between the CD4 pools of healthy, infected, untreated, and cART-treated animals.** CD4 pools in 3 groups of animals: uninfected healthy controls with PB CD4<sup>+</sup> T cell count > 600 cells/μl (black), advanced SIV chronically infected animals with PB CD4<sup>+</sup> T cell count < 300 cells/μl (blue), and SIV-infected long-term cART-treated (>5 months) nonhuman primates (red). Two animals in the group of SIV chronically infected animals were later treated with cART for more than 5 months: P246, who had 3 baseline scans during the chronic phase of infection (blue open circles) and before treatment (red open circle), and H755, who had 2 baseline scans during the chronic phase of infection (blue diamond with center dot) and was then reimaged after long-term treatment (red diamond with center dot). Another animal, P773, had 2 baseline scans during the chronic phase of infection (blue hexagon). Ax, axillary; Ing, inguinal; LN, lymph node; Sub, submandibular.

cART-treated animals ( $n = 6$ , mean PB CD4 count: 691 cells/μl, 95% CI, 235–1,147 cells/μl) had smaller axillary ( $P < 0.05$ ) and inguinal ( $P < 0.05$ ) LN CD4 pools but similar levels of submandibular and splenic CD4 pools (Figure 2). The suboptimal reconstitution of these clusters of LNs during long-term antiretroviral treatment is not consistently revealed by the PB CD4<sup>+</sup> T cell count, as can be seen for the SIV cART-treated animal P881 (Figure 3). Compared with advanced, chronically infected, and untreated animals (10 animals, 14 measurements, mean PB CD4<sup>+</sup> T cell count, 137 cells/μl; robust sample size adjusted GEE 95% CI, 87–186 cells/μl) (4, 5), the long-term treated animals had statistically significantly higher splenic and submandibular CD4 pools (linear mixed effects model,  $P < 0.01$ ) but similar levels of axillary and inguinal CD4 pools (Figure 2).

As evident from Figure 2, one animal in the treated group showed a supranormal level of CD4 pools in the axillary and inguinal LNs, about 2.5-fold higher than the healthy uninfected controls. Interestingly, this animal (P887) had a very high nadir PB CD4 count during the chronic phase of infection prior to initiation of cART (852 cells/μl compared with 43–498 cells/μl in the remaining 5 animals). Similarly, this supranormal level of CD4 pool in LNs was also observed in animals DCBP and P707, 2 SIV-infected animals with a long-term nonprogressor phenotype (Supplemental Table 1).

*Relationships between LTs and the PB CD4 pool in SIV-infected NHPs following the initiation or interruption of cART.* We next examined longitudinal changes in the images of the whole-body CD4 pool during administration of ART to a group of 7 SIV-infected animals. Five chronically SIV-infected animals (P248, H755, P246, P261, and P247) were imaged at baseline and at different time points following initiation of cART with <sup>99m</sup>Tc-F(ab)<sub>2</sub>-OKT4A. Similarly, 2 additional chronically SIV-infected animals (P844 and P773) were imaged at baseline and at different time points following initiation of cART with <sup>99m</sup>Tc-F(ab)<sub>2</sub>-CD4R1. The specific probes used for each imaging session and the imaging time points are indicated in Supplemental Table 2. Plasma samples were collected at each imaging time point and screened for immunogenicity to the probe. Data were excluded from the analyses if the animals developed an antibody response to the probe (Supplemental Data, Supplemental Figure 4).

As shown in the lower panels of Figure 3 and as expected, cART led to reductions in SIV RNA levels and increases in PB CD4<sup>+</sup> T cell counts in all animals. During the first month of therapy, the increase in PB CD4<sup>+</sup> T cell counts (mean 120 cells/μl; 95% CI, –31 to 271 cells/μl) was concomitant to a statistically significant increase

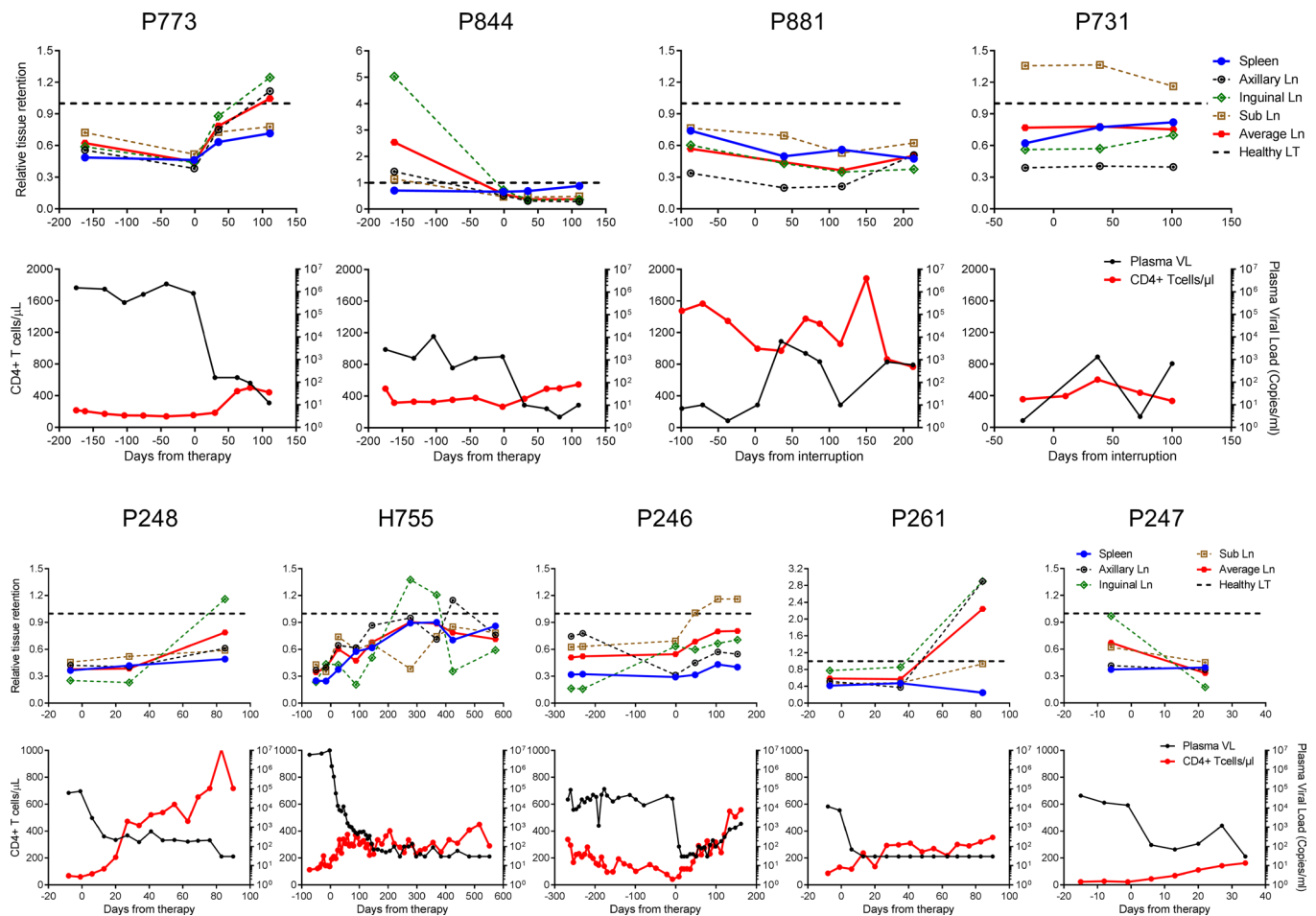


**Figure 3. Whole-body dynamics of the CD4 pool, CD4<sup>+</sup> T cell count, and plasma VL after cART initiation or interruption.** 9 monkeys were studied longitudinally following start of therapy or interruption. For each animal, top graph shows the relative radiotracer retention in lymphoid tissues calculated with respect to the mean levels measured in a group of healthy controls (horizontal dashed line), and bottom graph shows CD4<sup>+</sup> T cell count in the peripheral blood (cells/ $\mu$ L) and SIV RNA (copies/ml) in plasma. Day 0 indicates the start of therapy or interruption.

in the splenic pool of CD4<sup>+</sup> T cells (mean 19.6%, 95% CI, 2.6%–36.6%) ( $P < 0.05$ ,  $n = 7$ ). In the following months, however, additional increases in CD4<sup>+</sup> T cell counts were associated with variable degrees of change in tissue retention of tracer. In 2 animals (P248 and P261), there were marked increases of the CD4 pools in specific clusters of LNs with little change in splenic uptake. These 2 hosts also revealed an unexpected dynamic, with CD4<sup>+</sup> T cell reconstitution appearing in different LTs at different times. In P844, there was a marked increase in splenic uptake with no change in LN CD4 pools. Other animals (H755, P246, and P773) showed increases in both LNs and spleen. Overall, this group of animals illustrate that the dynamics of CD4 repopulation in LTs are only approximated by the dynamics of CD4 repopulation in the PB and that the reconstitution is highly heterogeneous not only among hosts, but also within different anatomic compartments of the same host.

As an example, animal H755 (Figure 3 and Figure 4) showed a rapid increase in the PB CD4 count during the first 4 weeks following initiation of cART, which then stabilized throughout the period of follow up to low levels (~300 CD4<sup>+</sup> T cells/ $\mu$ L). Surprisingly, the LTs showed a gradual repopulation that achieved close-to-normal levels within 1 year of follow up. In this case, the whole-body repopulation of the CD4 pool continued, despite a rapid plateau achieved in the PB compartment.

We next examined the changes in the CD4 pool following interruption of cART in 2 chronically SIV-infected animals. Animal P881 received cART for ~19 months, which led to a decrease in plasma viremia from ~5 log to <15 SIV RNA copies/ml for ~1 year prior to interruption of therapy. At the time of therapy interruption, the PB CD4<sup>+</sup> T cell count was above 1,300 cells/ $\mu$ L, and despite this normal PB CD4 count, splenic and LN CD4 pools were ~30%–40% of healthy controls (Figure 3 and Figure 5). Following interruption of cART, the PB CD4 count dropped during the first month by 34%, concomitant

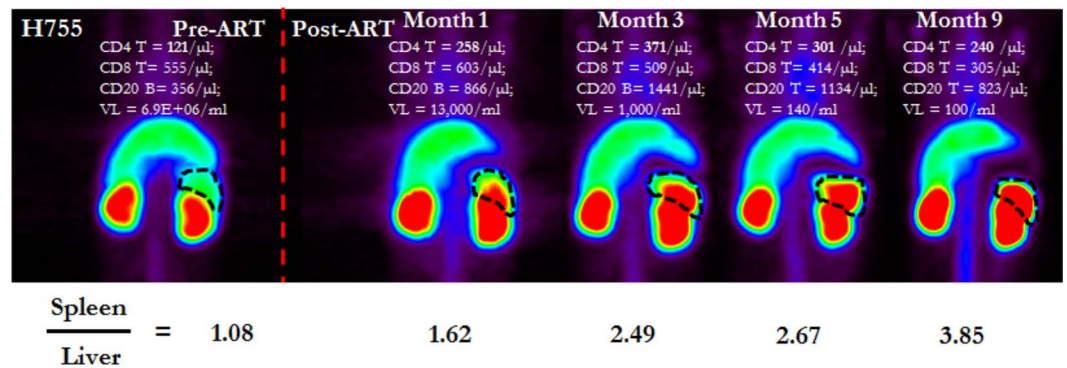


**Figure 4. cART-induced splenic CD4 pool repopulation in a poor immunologic responder.** Dynamics of cART-induced CD4 repopulation of the spleen in the SIV-infected animal H755. All images are adjusted on the maximum liver uptake. Dashed lines indicate spleen regions of interest.

with a 33% decrease in the splenic CD4 pool. Similarly, animal P731 received cART for ~18 months with a reduction in plasma viremia from ~4 log to <10 SIV RNA copies/ml for 1 year prior. At the time of therapy interruption, the PB CD4 T cell count was 355 cells/μl. The sizes of the splenic and most of the LN CD4 pools were below those of healthy controls (Figure 3). Surprisingly, following interruption of cART, we observed an increase (instead of a decrease) in CD4<sup>+</sup> T cell count 6 weeks following interruption of cART. This was accompanied by an increase in the splenic CD4 pool, with no appreciable changes in LN CD4 pools. The LTs did not show evidence of CD4 depletion during the following 2 months of therapy interruption, during which time plasma viral load remained below ~3 log.

*Images of gut CD4 pool.* Similar to what has been observed in our previous studies (1, 3), using either the <sup>99m</sup>Tc-F(ab')<sub>2</sub>-OKT4A or the <sup>99m</sup>Tc-F(ab')<sub>2</sub>-CD4R1 radiotracers, no differences were noted in the analyses of the 3D SPECT images of the intestines between healthy and SIV-infected CD4-depleted animals. This was despite observing significant differences in probe uptake in LNs and the spleen.

To further examine the relative uptake of the tracer in the LTs, we harvested LNs, splenic tissue, and gut tissue from control and CD4-depleted animals for ex vivo imaging following in vivo administration of probe. Two groups of animals, each group consisting of 1 healthy and 1 SIV-infected animal, were necropsied at 6 hours or 21 hours p.r.i., respectively, and organs were harvested for radioactive measurements. The organs were placed on a tray and imaged with the SPECT camera (Supplemental Figure 5 for the 6-hour p.r.i. necropsy, and Figure 6 for the 21-hour p.r.i. necropsy). As can be seen from the planar images of the trays in Figure 6, isolated discrete areas of high radiotracer uptakes can be seen in both the healthy and infected animals, with few of these discrete spots reaching levels similar to the uptake in the LNs. Of note, in the healthy animal, we identified 4 hot areas, with 3 of them localizing in the mesenteric compartment but not in the intestines. Overall, LN uptake was ~15-fold lower in the CD4-depleted animals compared with the controls. Few, if any, differences in gut radioactivity were observed between the healthy and the CD4-depleted animals.

## Discussion

Fewer than 2% of the total number of lymphocytes in the body reside in the PB at any time (1). Small changes in the distribution of lymphocytes between PB and tissues can have a significant impact on the number of CD4<sup>+</sup> T cells measured in 1 μl of blood. Hence, in vivo imaging technologies of the T cell pools may be able to provide a more robust quantitative analysis of the T cell pool under specific perturbations of the quasi-steady state of the immune system.

After describing the feasibility of imaging the CD4 pool in vivo using SPECT and an intact anti-CD4 mAb labeled with <sup>111</sup>Indium in healthy and SHIV-infected animals, our group has recently used the modified anti-CD4 radiotracer presented in this study (<sup>99m</sup>Tc-F(ab')<sub>2</sub>-CD4R1) to image the whole-body CD4 pool following conditioning regimen and autologous stem cell transplantation in rhesus macaques (3). These first studies also provided ex vivo measurements to validate the use of this noninvasive in vivo imaging system to infer the total number of CD4 cells in anatomic compartments. We provided evidence that the radiotracer uptake is proportional to the number of CD4 receptors per unit volume of tissue only in clusters of axillary,

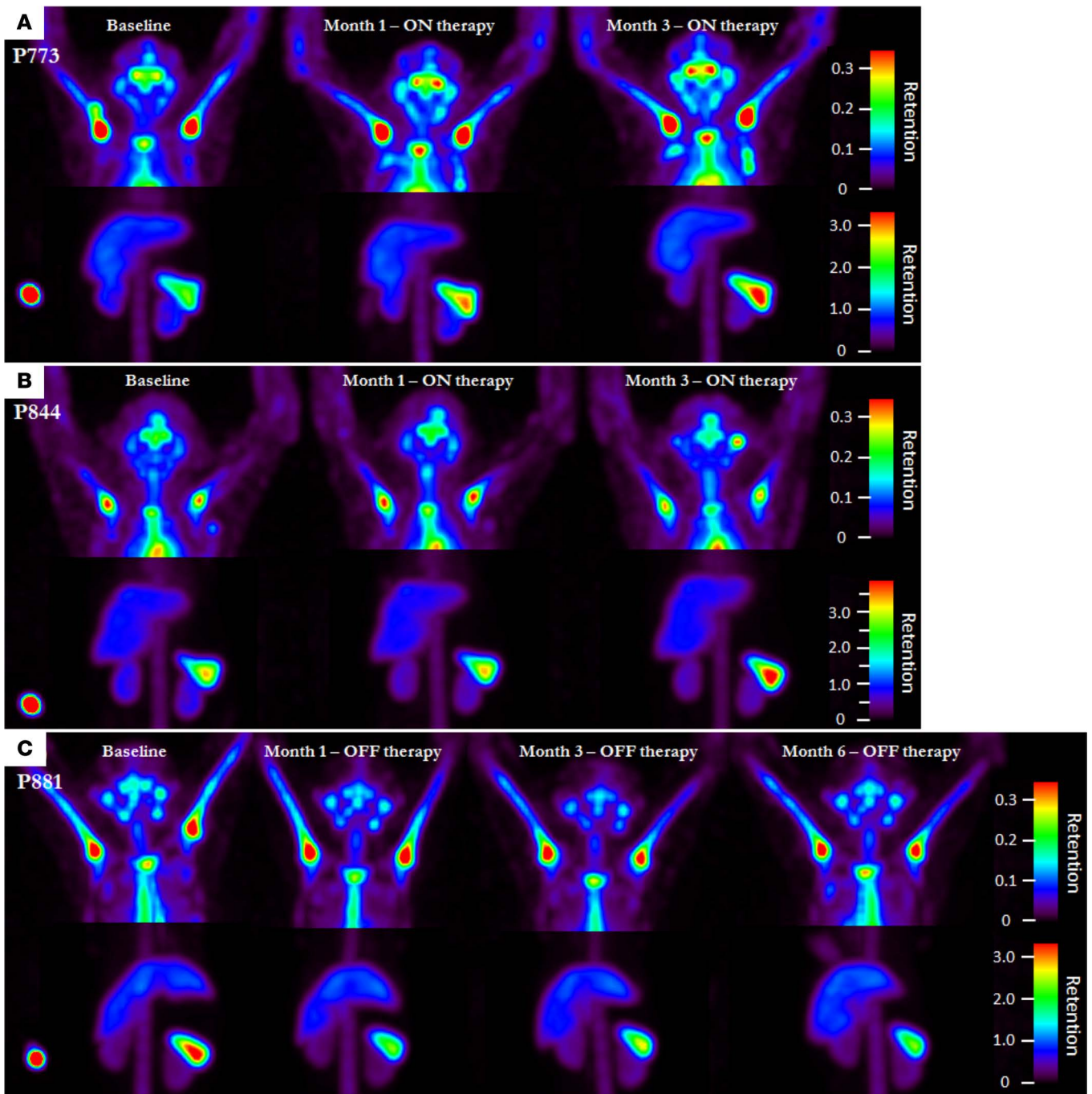


**Figure 5. Images of CD4 pools following initiation or interruption of cART.** LT CD4 pool dynamics following initiation (A and B) or interruption (C) of cART in 2 SIV-infected nonhuman primates. All images are adjusted within and between monkeys on the maximum liver uptake (for SPECT). Different image contrasts were applied to head and abdominal field of views (FOV) in SPECT image to highlight clusters of LNs and spleen. Tissue uptakes were converted to RAINBOW color scale as shown in color bar, where red indicates highest retention.

submandibular, and inguinal LNs, and in the spleen (i.e., in lymphoid organs with sufficient densities of CD4 receptors [number of receptors per unit volume] to be detected above background levels using this imaging system). Because, in these organs, more than 90% of the uptake was found to be the result of specific binding, it was possible to observe differences in these organs following perturbations of the immune system (e.g., after SIV infection or after initiation of ART) within a range of ~10-fold maximum differences between healthy and severely CD4-depleted animals. Conversely, in anatomic compartments with low densities of CD4 cells, the majority of the probe uptake is nonspecific; therefore, no correlation is observed

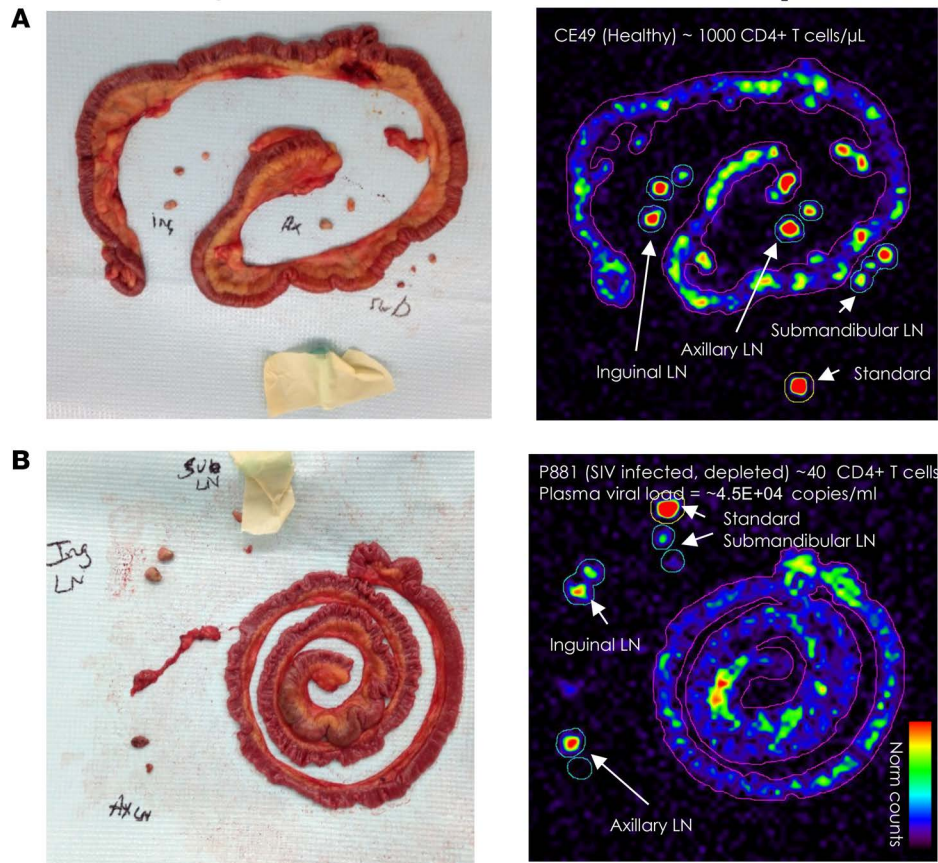


**Figure 6. Ex vivo imaging of the gut.** One healthy (A) and 1 SIV-infected (B) animal were necropsied at 21 hours p.r.i. The entire jejunum and entire ileum (>95% of the small intestines) and entire colon laid on a tray with a portion of the mesentery (~50% of the entire mesentery) attached to the intestine walls. The mesentery is a double fold of peritoneum, fan-shaped, which covers the entire length of the jejunum and ileum. Between the 2 leaves of the mesentery are the mesenteric vessels, fat, and mesenteric lymph nodes. Tissue uptakes normalized on plasma levels were converted to RAINBOW color scale as shown in color bar, where red indicates highest uptake.

between the latter and the state of immunodeficiency of the host. An example is the PB, in which the number of CD4 cells per unit volume can be 100 fold or more different between healthy and SIV-depleted animals, yet no difference in anti-CD4 probe uptake is observed throughout the imaging biodistribution period.

The new radiotracers produced higher quality images of the whole-body CD4 pool due to the lower backgrounds. The highest levels of radiotracer uptakes were observed in the clusters of LNs and in the spleen of healthy animals, and — similar to the intact anti-CD4 mAb — these were positively correlated with the PB CD4<sup>+</sup> T cell count. Moreover, as expected, no correlations were found between the radiotracer uptake in organs of clearance (e.g., kidney and liver) and the PB CD4<sup>+</sup> T cell count. In vivo and ex vivo radioactivity data did not reveal differences in anti-CD4 radiotracer uptake in the gut, despite changes in PB CD4 counts.

The transplant study also showed that dramatic fluctuations of the number of CD4<sup>+</sup> T cells in the PB can occur by forcing the release of lymphocytes from the LTs to the PB with agents such as the CXCR4 receptor antagonist AMD3100, without detectable changes in the whole-body CD4 pool. This observation is consistent with a small percentage of CD4<sup>+</sup> cells in tissues being released from tissues to PB following AMD3100 administration and highlights the importance of whole-body CD4 imaging to assess the etiological factors behind the fluctuations of CD4 cells in the PB; therefore, the use of this technology is particularly important when we perturb the immune system with immunotherapeutic strategies that are known to interfere with homing and trafficking of lymphocytes in the body.

In vivo imaging of the CD4 pool has recently been used to help discern the effects of an anti- $\alpha\beta 7$  mAb on the SIV reservoir and CD4 pool (6), an example of immunotherapeutic strategy that is expected to perturb trafficking of lymphocytes between tissues and PB. In that study, using the same antibody fragment

utilized in this study and in our previous work (3), the authors noted similar biodistribution of the probe in the LNs and spleen but noted a high uptake of the probe in the gut of healthy animals from in vivo imaging data (with a mean probe uptake throughout the gut similar to the probe uptake in the LNs). The reasons behind this striking difference between that study and our observations are unclear but may include the use of different radiolabeling procedures ( $^{99m}\text{Tc}$  versus  $^{64}\text{Cu}$ ), different biodistribution periods (21 hours versus 36 hours), or use of a higher ( $\sim 100\ \mu\text{g}$  versus  $\sim 1\ \text{mg}$ ) dose of tracer leading to differential organ-specific penetration of the probe (Supplemental Data, and Supplemental Figures 7–9). Alternatively, the high gut uptake reported in Byrareddy et al. (6) could be primarily explained by uptake in mesenteric LNs (in proximity to the intestinal walls) as opposed to the gut. The mesenteric LNs are distributed in a larger volume of interest (VOI) compared with the clusters of axillary, inguinal, or submandibular LNs, hence the 2 sets of studies may be reconciled by the differential spatial resolutions of the in vivo imaging technologies adopted (PET superior to SPECT), as could be revealed by ex vivo measurements of the intestines harvested on a tray in which the contribution of mesenteric LNs would be minimized. In order to address this major discrepancy between the 2 sets of studies, we have studied the biodistribution of the  $^{64}\text{Cu}$  anti-CD4 probe and found that the  $^{64}\text{Cu}$  and the  $^{99m}\text{Tc}$  probes show similar biodistributions (from ex vivo measurements) when injected at the same dose, excluding differential penetration as the major factor behind the differences observed in the 2 studies and providing evidence that the mean uptake of the probes in the intestinal walls is about 10-fold lower than the probe uptake in the LNs (Supplemental Figure 9). Consistent with our conclusions, dose-escalating studies of a different anti-CD4 fragment probe to image the CD4 pools, recently described in rodents (7), showed that, despite increasing the total mass of the probe injected, the relative uptake in the small and large intestines remains low and  $\sim 50$ -fold lower than the relative probe uptake in spleen and clusters of LNs. To fully resolve this important discrepancy, dose-escalating studies in NHPs of the anti-CD4 probe are needed to optimize the dose administration for the CD4 pool imaging system in large hosts (8), as well as to confirm the nature of the probe uptake in the gut ROI. The generation of an input function and time activity curve for a precise estimate of the binding potential for CD4 receptors in the organs of interest are needed to reconcile these observations and to identify the optimal dose and timing of imaging, for the efficient translation of this technology to human studies (9).

The imaging system in the present study highlighted a nonlinear relationship between the PB and LT pools of CD4<sup>+</sup> T cells similar to what was observed with the intact anti-CD4 mAb (1). One possible explanation for this is that partition of CD4 cells between PB and LT changes at different CD4 pool sizes. This explanation is consistent with previous observations in SIV-infected monkeys (10) in which more dramatic changes in the CD4 pool of LNs have been reported to occur when the CD4<sup>+</sup> T cell count in the PB falls below 200–300 CD4<sup>+</sup> T cells/ $\mu\text{l}$ , suggesting that trafficking rates between PB and LTs are not constant but are governed by incompletely understood mechanisms, possibly related to lymphoid homeostasis.

The potentially novel anti-CD4 radiotracer used in this study cannot discriminate between CD4<sup>+</sup> T cells and other CD4<sup>+</sup> cells such as macrophages. The latter cells express CD4 at relatively low levels per cell compared with lymphocytes (11, 12). Moreover, the percentage of mononuclear cells (MNCs) that are macrophages is much lower than lymphocytes in spleen and LNs (13). Therefore, the contribution to the total binding sites for the radiotracer (i.e., CD4 receptors per unit mass/volume of tissue) brought by the macrophages/monocytes compartment is expected to be much lower than the contribution brought by the CD4<sup>+</sup> T cells.

The fragmentation of intact anti-CD4 mAbs into a less immunogenic tracer has also allowed longitudinal imaging of the CD4 pools in rhesus macaques infected with SIV following initiation and discontinuation of ART. As expected, in cross-sectional analyses of quasi-steady states of the immune systems of hosts imaged at different phases of disease progression, highly significant associations have been found between the PB CD4 count and the CD4 pools of LNs and spleen. The imaging system also provided some evidence of suboptimal reconstitution in specific clusters of LNs, but not in the spleen, in the settings of long-term cART-treated animals, including in 1 animal with normalized PB CD4 count. Interestingly, this slower reconstitution of the CD4 pool in clusters of LNs compared with spleen was also observed following total body irradiation and autologous stem cells transplantation. In that study, complete reconstitution of the PB CD4<sup>+</sup> T cell counts and splenic CD4 pools were seen in a setting of only 60%–70% recovery of the LN CD4 pools. Of note, SIV/SHIV infection appears to cause a more complete depletion of the total body CD4 pool compared with medium to high doses of total body irradiation (3).

This profound heterogeneity in immune reconstitution among anatomic compartments observed following cART in the SIV model may reflect different degrees of damage and fibrosis to secondary lymphoid organs

with tissue-specific disruption of lymphoid repopulation (14). Alternatively, slower reconstitution in specific anatomic compartments could also reflect localized persistent residual immune activation, caused by residual viral production with or without de novo infection due to poor or suboptimal penetration of antiviral drugs to sanctuary sites such as LNs (15–17) or to the differential impact of foreign antigens in different LNs.

Interestingly, in a multivariate analysis with repeated measurements of all infected longitudinally imaged animals, we found evidence that, after adjusting for PB CD4 counts, plasma viremia was still independently associated with the CD4 pool of the spleen but not with the CD4 pool of the LNs.

The spleen is the largest reservoir of lymphocytes in the body (1, 18). It is of note that a statistically significant increase in the splenic CD4 pool was seen as early as 4 weeks after the initiation of ART. These data indicate that the early phase of increasing CD4<sup>+</sup> T cell counts seen following initiation of cART may be due to more than just changes in trafficking rates between LTs and PB. Similarly, the rapid declines in CD4<sup>+</sup> T cell counts seen following discontinuation of cART were immediately reflected in the spleen. Overall, gains (up to 37%) in the splenic CD4 pool happen as rapidly as losses (up to 30%) in the splenic CD4 pool 4 weeks following initiation or interruption of cART, respectively.

Overall, our data suggest that the dynamics of the CD4<sup>+</sup> cell pool following initiation or interruption of ART in SIV-infected NHPs are only approximated by the dynamics observed in PB CD4 counts and appear highly heterogeneous between and within hosts. A key example of mismatch in the dynamics of cART-induced CD4 reconstitution between the PB and LT is offered by animal H755, in which a plateau in the number of CD4 cells in the PB is reached several months earlier than the LT. This host also illustrates the fact that low CD4<sup>+</sup> cell counts in the blood, does not exclude close-to-normal reversion of HIV-induced immunodeficiency at the tissue level, suggesting that at least some of the patients with treated HIV infection referred to as poor immunologic responders may in fact have normal immune systems at the tissue level (19). Applying these techniques of in vivo imaging to humans would directly test this hypothesis.

Our data are also consistent with a seemingly stochastic pattern of LN regeneration following cART (i.e., changes in the CD4 pools of the LNs do not appear to be synchronous or homogeneous between hosts or within anatomic compartments of the same host). In some animals, increases in the CD4 pool following initiation of cART take place in specific clusters of LNs but not in other clusters or in the spleen. In other animals, visible increases in the CD4 pool of LNs can be seen at month 1, while in other animals, longer treatment periods are needed for CD4 levels to increase. Whether irreversible or partially reversible LN elasticity induced by SIV replication in tissues is in part responsible for the seemingly stochastic LNs in CD4 pool reconstitutions deserves further investigation (20). Whole-body imaging-guided sampling of tissues in future longitudinal analyses may provide important insights on the etiological factors behind differential organ-specific reconstitution or depletion of the T cell pools, following specific perturbations of the quasi-steady state of the immune system.

The sample size and limited number of radiotracer administrations, due to the development of immunogenic response to the tracer, constitute the major limitations of the current study. It is relevant to note that the outcome of the in vivo imaging is a measurement for the receptor density of an entire organ — therefore, less vulnerable to sampling variabilities. Based on consecutive imaging sessions, performed only a few weeks apart in animals at steady state, these measurements are quite reproducible (Figure 3). The extension of this technology to imaging of humans (e.g., through the radiolabeling of fully humanized anti-CD4 mAb fragments; ref. 21) or the design of nonimmunogenic low molecular weight anti-CD4 radioprobes may help to better gauge the degree of immune reconstitution following standard and experimental treatments of HIV. Imaging of the CD4 pool of humans may allow for better evaluation of immune reconstitution in the settings of HIV infection and other conditions associated with CD4 depletion.

## Methods

### Preparation of <sup>99m</sup>Tc-labeled anti-CD4 tracers

**Antibodies.** Humanized anti-CD4 CDR-OKT4A/huIgG4 was produced from transfected NS0 cells as previously described (22). To produce rhesus recombinant antibody, CD4R1-OKT4A/rhIgG1, complementarity determining regions (CDRs) representing the anti-CD4 antibody OKT4A (23) were grafted onto a rhesus scaffold using rhesus germline variable region as templates. Key positions potentially contributing to antigen binding, CDR conformation, and heavy- and light-chain interactions were retained as the mouse residue (24). DNA representing recombinant variable heavy regions ( $V_H$ ) and variable light regions ( $V_L$ ) were synthesized, amplified by PCR, and purified from agarose gel with the QIAquick Gel Extraction Kit

(Qiagen). Recombinant fragment variable DNAs (Fv-DNAs) were subcloned into rhesus IgG1 constant heavy region ( $C_H$ ) and constant light region ( $C_L$ ) expression vectors as described above. For large-scale production of rhesus recombinant antibodies, recombinant heavy- and light-chain vectors were packaged in retroviral vectors and used to infect CHO cells using the GPEx expression platform (Catalent Pharma Solutions). Antibody was produced from a high-expressing transduced subclone, grown in serum free medium. After clarification, recombinant antibody was purified from supernatant by protein A affinity chromatography. The purified antibodies were placed in phosphate buffer, pH 6.5. Endotoxin levels were <1 EU/mg of antibody.

**Preparation of  $F(ab')_2$ .** We prepared  $F(ab')_2$ -OKT4A and  $F(ab')_2$ -CD4R1 by pepsin digestion according to the manufacture's instruction (Pierce  $F(ab')_2$  Preparation Kit, Thermo Fisher Scientific). Briefly, 20 mg of CDR-OKT4A/huIgG4 (5 mg/ml) or CD4R1-OKT4A/rhIgG1 (5.1 mg/ml) was digested by pepsin immobilized on agarose gel (Thermo Fisher Scientific) in 0.1 M sodium acetate buffer (pH 4.4). The digestion was performed at 37°C for 4 hours using an optimal antibody/pepsin weight ratio between 6.7:1 to 10:1. After digestion, the reaction mixture was purified using Protein A-Sepharose affinity chromatography (Thermo Fisher Scientific), followed by dialysis in PBS using a dialysis membrane cassette with 20 kDa molecular weight cut-off at 4°C for 22 hours. The purified protein was concentrated using a Centrprep YM-50 membrane (Amicon) to a concentration of 5.2 mg/ml. Protein purity was assessed by SDS-PAGE (Invitrogen) and size-exclusion HPLC (Gilson) equipped with a size-exclusion TSK gel G3000SW<sub>XL</sub> column (7.8 × 300 mm, 5 μm, TOSOH Bioscience; 0.067 M sodium phosphate/0.15 M sodium chloride with, pH 6.8; 1.0 ml/min) and a UV monitor.

**Conjugation of HYNIC to  $F(ab')_2$ -OKT4A and  $F(ab')_2$ -CD4R1.** Succinimidyl-6-hydrazino-nicotinamide (HYNIC-NHS, Solulink) was freshly dissolved in DMF (5.2 mM). Ten times molar excess (200 μmol) of HYNIC-NHS was added to 2 mg (20 μmol) of  $F(ab')_2$  fragments in 0.4 ml of 0.0067 M PBS buffer (PBS 1×), pH 7.2. The solution was stirred gently and incubated in a refrigerator at 4°C for 65 hours. The level of HYNIC conjugation was estimated to be 3 HYNIC molecules per  $F(ab')_2$  by the percent distribution of <sup>99m</sup>Tc between HYNIC- $F(ab')_2$  and free HYNIC when analyzed by size-exclusion HPLC. The reaction mixture was diluted 10 times with the same PBS and concentrated by Amicon 50K. The protein concentration was determined by the Bradford method. The conjugated product was stored in a freezer at -80°C until radiolabeling with <sup>99m</sup>Tc for imaging studies.

**<sup>99m</sup>Tc labeling.** In a rubber-sealed vial, HYNIC- $F(ab')_2$ -OKT4A or -CD4R1 (360 μg in PBS 1×) was incubated with <sup>99m</sup>TcO<sub>4</sub><sup>-1</sup> (40 mCi; 1480MBq) in 0.2 ml aqueous medium at pH 6 containing tricine (112 mM, 20 mg/ml), sodium succinate (25 mM), and stannous chloride (82 μg/ml) at 37°C for 30 minutes. All reagents were freshly made in deionized water, which was deoxygenized by bubbling with N<sub>2</sub> stream for 1 hour. <sup>99m</sup>Tc labeled  $F(ab')_2$  proteins were purified on PD-10 size-exclusion columns (GE Healthcare) eluted with PBS, pH 7.2. The radiochemical purity of the <sup>99m</sup>Tc-labeled  $F(ab')_2$  was determined by size-exclusion HPLC equipped with an on-line flow radioactivity detector (BioScan).

### Immunoreactivity binding assays

The immunoreactivity of the radiolabeled products was tested using a modification of a cell-binding assay by Lindmo and Bunn (25), as previously described (1).

### Animals study design

**Healthy animals and SIV-infected animals before/after cART treatment, imaged with <sup>99m</sup>Tc- $F(ab')_2$ -OKT4A.** An outline of the protocol design and the number of adult monkeys (median age 6.2 years [5–13.8 years] and median weight 6.9 kg [5.4–11.8 kg]) imaged with the humanized <sup>99m</sup>Tc- $F(ab')_2$ -OKT4A at different phases of lentiviral infection are shown in Supplemental Tables 1 and 2. Two uninfected female (CE7E, 01D278), 3 uninfected male (CF67, XAW, DBPN), 1 SIV-thymidine kinase-infected (SIV-TK-infected) male (A5E036), 1 SIVE543-infected male (H755), and 4 SIVmac251-infected females (P246, P261, P248, P247) Indian rhesus macaques were imported in this study from 3 completed studies at NIH. The SIVmac251-infected animals were transferred from a study, and these animals received a recombinant vaccine containing canarypox vector-SIV (ALVAC-SIV) 1 year prior to importing them in our study (26). The SIV-TK-infected rhesus macaque was challenged i.v. with 1 × 10<sup>5</sup> TCID50 of a recombinant SIVmac239 virus carrying the HSV-TK gene in Nef and showed complete control of viral load and high levels of CD4 cell counts after the phase of acute infection. The SIVE543-infected rhesus macaque was challenged intrarectally with 1 × 10<sup>3</sup> TCID50 of

SIVsmE543-3 (27). The P246, P248, and P247 rhesus macaques were challenged with  $1 \times 10^4$  TCID50 and the P261 with  $2.0 \times 10^3$  TCID50 of SIVmac251, intravaginally. Following baseline imaging, the SIVE543-infected animal and the 4 SIVmac251-infected animals were treated with cART: Tenofovir (PMPA) 20 mg/kg + Emtricitabine (FTC) 50 mg/kg, s.c. once per day. All animals utilized in this study were maintained in accordance with the Guide for the Care and Use of Laboratory Animals (28). They were housed in a biosafety level 2 facility, and biosafety level 3 practices were followed. Phlebotomies and virus inoculation were performed with animals anesthetized with ketamine/acepromazine.

*Healthy animals and SIV/SHIV-infected animals imaged with  $^{99m}\text{Tc-F(ab)'}_2\text{-CD4R1}$ .* An outline of the protocol design and the number of adult monkeys (median age: 4.2 years [3.1–9.9 years] and median weight: 5.4 kg [4.4–9.2 kg]) imaged with the rhesus recombinant  $^{99m}\text{Tc-F(ab)'}_2\text{-CD4R1}$  are shown in Supplemental Tables 1 and 2. Seven uninfected and 12 lentiviral (SIVmac251, SIVmac239, SHIVAD08, SHIVDH12R) chronically infected Indian rhesus macaques were recruited in this study. The SIVmac251-infected rhesus macaques were challenged intrarectally with  $1 \times 10^3$  TCID50 of SIVmac251. The SHIV-infected rhesus macaque, DA24, was challenged intrarectally with 10 TCID50 of SHIVAD8 clone (29). The SIV-TK-infected rhesus macaque (A5e006) was challenged i.v. with  $1 \times 10^5$  TCID50 of a recombinant SIVmac239 virus carrying the HSV-TK gene in Nef and showed complete control of viral load and high levels of CD4 cell counts after the phase of acute infection. The SHIVDH12R/SIVmac239 chronically infected rhesus macaque, G43, was challenged i.v. with  $1 \times 10^3$  TCID50 of SHIVDH12R-clone 7 and  $1 \times 10^3$  TCID50 of SIVmac239. Following baseline imaging, 2 SIVmac251-infected animals (P844 and P773) were treated with Tenofovir (PMPA) 20 mg/kg + Emtricitabine (FTC) 30 mg/kg s.c. once per day, and Raltegravir 20 mg/kg/BID mixed in food. The SIVmac251-infected animals (P881 and P731) were both treated with the same regimen when they were imaged at baseline, prior to interruption of cART.

### Lymphocyte immunophenotyping and plasma viral RNA measurements

Virion-associated SIV RNA in plasma was measured using a quantitative PCR (qPCR) assay, essentially as described previously (30). Immunophenotyping of EDTA-treated blood samples was carried out by using fluorochrome-conjugated mAb (anti-CD3-fluorescein isothiocyanate, 556611; anti-CD4-allophycocyanin, 340443; anti-CD8-peridinin chlorophyll protein, 347314; anti-CD20-phycoerythrin-CY7, 335793; and anti-Ki67-phycoerythrin, 556027; all BD Biosciences) and analyzed by flow cytometry (31).

### Imaging and Biodistribution Studies (SPECT/CT)

The animals were anesthetized with ketamine (10 mg/kg) and acepromazine (VetOne) (0.1 mg/kg) and, after shaving the skin and prepping the insertion sites, a 22-gauge catheter was inserted in the saphenous vein of the leg for the administration of radiotracer or for administration of anesthetics during the imaging procedures. Anesthetized primates were monitored with pulse oxymeter and thermometer. Heating pads were used to maintain the animal's body temperature during imaging. The arms and legs of the macaque were restrained, and the animals were positioned in the appropriate orientation for imaging. Animals in the cross-sectional group analysis of the humanized anti-CD4 fragment received an average dose of 6.04 mCi (4.01–8.23 mCi) of  $^{99m}\text{Tc-F(ab)'}_2\text{-OKT4A}$  as described in Supplemental Table 1. Animals in the cross-sectional group analysis of the rhesus recombinant anti-CD4 fragment received an average dose of 6.12 mCi (4.34–9.04 mCi) of  $^{99m}\text{Tc-F(ab)'}_2\text{-CD4R1}$  as described in Supplemental Table 1. Animals in the longitudinal cART-group analysis were imaged at multiple time points as described in Supplemental Tables 1 and 2. Serial scintillation camera images were acquired with a triple-headed SPECT camera (Triad88, Trionix) or a dual-headed SPECT-CT camera (Symbia T2, SPECT/CT Siemens), at 4 and (in a subgroup of animals) at 19 hours p.r.i. The images were obtained with a low-energy high-resolution (LEHR) collimator. Individual anterior whole-body images and whole-body SPECT images were recorded for visual and semiquantitative analyses of radiotracer uptakes. All images were interpreted by an experienced nuclear medicine physician. SPECT images were analyzed by manually drawing consecutive ROI over the transverse sections of the heart; liver; kidney; bone marrow (positioned over the head and proximal segment of the humerus); thymus; submandibular, axillary, and inguinal LNs; and the spleen to cover the entire volume of the organs (VOI). The VOI for the submandibular LNs may also include the salivary glands. The coregistration of CT and SPECT images was produced in animals imaged with the Symbia T2 (SPECT/CT) camera and was used to confirm the VOI of the above organs. Semiquantitative analysis of SPECT images was performed on SPECT (3D-reconstructed) and whole-body images obtained at 4 hour p.r.i., to estimate the relative uptake of radiotracers in different organs. Images were not corrected for partial volume effect (PVE).

The radiotracer uptake, also called radiotracer retention, for each VOI was obtained from the maximum activity in the VOI normalized on the maximum activity in the liver. In addition, hepatic and other tissue radiotracer uptakes were measured as standardized uptake value ( $SUV_{max} = [C/ID] \times w$ ) from the SPECT images (1), where  $C$  is the decay-corrected maximum counts converted in  $\mu\text{Ci}/\text{ml}$  using the imaging standard in the VOI, and  $ID$  and  $w$  are the injected dose (expressed in  $\text{mCi}$ ) and body weight (expressed in  $\text{Kg}$ ), respectively. The relative radiotracer retention in LTs was calculated with respect to the mean levels measured in a group of healthy controls with  $\text{CD4}^+$  T cell counts  $> 600$  cells/ $\mu\text{l}$ . At the end of each imaging study, 500  $\mu\text{l}$  of blood was withdrawn for plasma radioactivity counting in the  $\gamma$  counter. The plasma SUV was derived multiplying the percentage of injected dose by the animal weight.

### Specificity of binding in vivo

Specificity of binding in vivo was tested in axillary, inguinal, and submandibular LNs extracted from 2 animals at 6 hours following  $^{99\text{m}}\text{Tc-F(ab')}_2\text{-CD4R1}$  injection or from 1 monkey at 19 hours after the administration of the ( $^{99\text{m}}\text{Tc-F(ab')}_2\text{-OKT4A}$ ) radiotracer. LNs were mechanically disrupted by pressing through a 70- $\mu\text{m}$  pore-size cell strainer (Thermo Fisher Scientific). Erythrocytes were lysed with ACK lysing buffer (BioWhittaker), and cells were washed with complete RPMI medium. Cells were stained with trypan blue to obtain the number of total viable cells.  $\text{CD4}^+$  cells were isolated using Miltenyi MiniMACS Separator (Miltenyi Biotec), per manufacturer's instructions. Isolated cells were resuspended in 1 ml of PBS, and the radioactivity was counted in the  $\gamma$  counter.

Two additional groups of 2 animals each were euthanized at 6 hours and 21 hours, following  $^{99\text{m}}\text{Tc-F(ab')}_2\text{-CD4R1}$ , and large sections of the jejunum and colon — as well as of other organs — were harvested, placed on a tray, and imaged with the SPECT camera. Small aliquots of these organs were also counted with the  $\gamma$  counter. Each group consisted of 1 healthy and 1 SIV-infected animal with high and low PB  $\text{CD4}^+$  T cell count, respectively. The SIV-infected animal necropsied at 21 hours p.r.i. was also administered an anti-CD3 immunotoxin to further deplete the CD4 pool in tissues (32). These animals also underwent axillary and rectal mucosal biopsies at 3 hours p.r.i.

### Immunogenicity assays

Plasmas at each imaging time point were screened for antibodies to the probe by 3 independent assay, and data were excluded from the analyses if animals developed an anti-CD4 immune response. Three independent assays were performed to assess immunogenicity: radio-HPLC analysis, MT4 cell binding assay with plasma preincubated with the radiotracer, and ELISA. Aliquots of  $^{99\text{m}}\text{Tc-F(ab')}_2\text{-OKT4A}$  or  $^{99\text{m}}\text{Tc-F(ab')}_2\text{-CD4R1}$  were incubated in monkey plasma to reach concentration similar to plasma concentration at 4 hours p.r.i. ( $\sim 0.1$  ng/ $\mu\text{l}$ ) for 30 minutes at 37°C in a humidified 5%  $\text{CO}_2$  incubator. Aliquots (each 100  $\mu\text{l}$ ) of incubated samples were analyzed by size-exclusion HPLC equipped with an on-line flow radioactivity detector as described above. Another aliquot (20  $\mu\text{l}$ ) of the radiotracer-plasma incubation mixture was dispensed in 2 million MT4 cells for plasma cell binding assay for 90 minutes at 4°C. After incubation, the wells were washed, and the percentage of total activity bound to cells was determined in the  $\gamma$  counter (Wizard). The presence of anti-Ig responses directed against the anti-CD4 in the plasmas of rhesus monkeys was also determined by ELISA using 96-well plates coated with the parent CDR-OKT4A/huIgG4 or its digested  $\text{F(ab')}_2\text{-OKT4A}$ . A secondary mouse anti-human  $\lambda$  light chain conjugated to biotin (Miltenyi Biotec) and streptavidin/HRP system was used to detect binding of monkey IgG to the immobilized antigens. ELISA plates were washed to remove unbound detection antibodies, followed by incubation with tetramethylbenzidine (TMB) as a substrate. Enzymatic products were measured by an ELISA plate reader at 450 nm. Positive detection is defined as OD that is at least twice the baseline value (preradiotracer injection).

### Statistics

Linear mixed effect models, accounting for repeated measures by a random intercept per animal, were used for all the longitudinal analyses. One-tailed greater-than Spearman rank correlation test (using Winstat) was used to assess the relationship between variables in cross-sectional analyses; Wilcoxon rank sum tests were used to compare groups in Figure 2, when animals had repeated measurements (around the same time point used in the cross-sectional analysis). One measurement was selected for each animal. The total number of possible combinations for this selection process was used to obtain a  $P$  value for comparison as described in ref. 33. Other analyses were performed in R (34); mixed-effects modeling for the longitudinal

analysis used the *Lme4* and *lmerTest* packages (35, 36). A linear generalized estimating equation, with small sample size adjusted, was used to calculate means and robust 95% CI when there were repeated measurements for the same time point for any of the animals (GEE and SAWS packages in R; refs. 4, 5).  $P < 0.05$  was considered statistically significant.

### Study approval

The animal studies were performed under an approved IACUC (NIAID ACUC, Bethesda, Maryland, USA). All animals utilized in this study were maintained in accordance with the *Guide for the Care and Use of Laboratory Animals* (National Academies Press, 2011).

### Author contributions

MDM and SS designed and performed the research, analyzed/interpreted the data, made the figures, and cowrote the paper; IK designed and performed the research and analyzed/interpreted the data; GD, ASC, PD, MSC, and KAR performed research and analyzed/interpreted data; EEG, JC, RCR, and CP analyzed/interpreted data; HCL designed research, analyzed/interpreted data, and cowrote the paper. All coauthors critically reviewed the paper. The authors have declared that no conflict of interest exists.

### Acknowledgments

The content of this publication does not necessarily reflect the views or policies of the Department of Health and Human Services, nor does mention of trade names, commercial products, or organizations imply endorsement by the US. This project has been funded in part with federal funds from the National Cancer Institute, NIH, under contract no. HHSN261200800001E. We thank the animal care staff and technicians at the NIH Animal Facility in Poolesville (Maryland, USA) for their care and handling of the animals, and we thank Anthony Fauci for his support and guidance. We would also like to thank Kenneth Cheng of Clinical Center for radiopharmacy support, Russ Byrum from Battelle/Integrated Research Facility of Division of Clinical Research for veterinary support, and the Nonhuman Primate Reagent Resource, which is supported by NIAID contract no. HHSN27220130031C and grant OD0190976. We thank Merck for providing raltegravir and Gilead for providing tenofovir and emtricitabine.

Address correspondence to: Michele Di Mascio, Division of Clinical Research, National Institute of Allergy and Infectious Diseases, The NIH, Department of Health and Human Services, Rockville, Maryland, USA. Phone: 1.240.669.5262; Email: mdimascio@niaid.nih.gov.

- 
1. Di Mascio M, et al. Noninvasive in vivo imaging of CD4 cells in simian-human immunodeficiency virus (SHIV)-infected non-human primates. *Blood*. 2009;114(2):328–337.
  2. Pakker NG, et al. Biphasic kinetics of peripheral blood T cells after triple combination therapy in HIV-1 infection: a composite of redistribution and proliferation. *Nat Med*. 1998;4(2):208–214.
  3. Donahue RE, et al. Discordance in lymphoid tissue recovery following stem cell transplantation in rhesus macaques: an in vivo imaging study. *Blood*. 2015;126(24):2632–2641.
  4. Carey VJ. *gee: Generalized Estimation Equation Solver*. CRAN-R. <https://CRAN.R-project.org/package=gee>. Published June 29, 2015. Accessed June 26, 2018.
  5. Fay MP, Graubard BI. Small-sample adjustments for Wald-type tests using sandwich estimators. *Biometrics*. 2001;57(4):1198–1206.
  6. Byrreddy SN, et al. Sustained virologic control in SIV+ macaques after antiretroviral and  $\alpha\beta 7$  antibody therapy. *Science*. 2016;354(6309):197–202.
  7. Freise AC, Zettlitz KA, Salazar FB, Lu X, Tavaré R, Wu AM. ImmunoPET Imaging of Murine CD4+ T Cells Using Anti-CD4 Cys-Diobody: Effects of Protein Dose on T Cell Function and Imaging. *Mol Imaging Biol*. 2017;19(4):599–609.
  8. Sanders-Bear BE, Voronin Y, McDonald D, Singh A. Harnessing Novel Imaging Approaches to Guide HIV Prevention and Cure Discoveries-A National Institutes of Health and Global HIV Vaccine Enterprise 2017 Meeting Report. *AIDS Res Hum Retroviruses*. 2018;34(1):12–26.
  9. Zhang Y, Fox GB. PET imaging for receptor occupancy: meditations on calculation and simplification. *J Biomed Res*. 2012;26(2):69–76.
  10. Rosenberg YJ, et al. Variation in the CD4+ and CD8+ populations in lymph nodes does not reflect that in the blood during SIVMNE/E11S infection of macaques. *J Med Primatol*. 1992;21(2-3):131–137.
  11. Lewin SR, Sonza S, Irving LB, McDonald CF, Mills J, Crowe SM. Surface CD4 is critical to in vitro HIV infection of human alveolar macrophages. *AIDS Res Hum Retroviruses*. 1996;12(10):877–883.
  12. Thomas ER, et al. Macrophage entry mediated by HIV Envs from brain and lymphoid tissues is determined by the capacity to use low CD4 levels and overall efficiency of fusion. *Virology*. 2007;360(1):105–119.

13. Blackley S, et al. Primary human splenic macrophages, but not T or B cells, are the principal target cells for dengue virus infection in vitro. *J Virol.* 2007;81(24):13325–13334.
14. Zeng M, et al. Cumulative mechanisms of lymphoid tissue fibrosis and T cell depletion in HIV-1 and SIV infections. *J Clin Invest.* 2011;121(3):998–1008.
15. Di Mascio M, et al. Antiretroviral tissue kinetics: in vivo imaging using positron emission tomography. *Antimicrob Agents Chemother.* 2009;53(10):4086–4095.
16. Lorenzo-Redondo R, et al. Persistent HIV-1 replication maintains the tissue reservoir during therapy. *Nature.* 2016;530(7588):51–56.
17. Fletcher CV, et al. Persistent HIV-1 replication is associated with lower antiretroviral drug concentrations in lymphatic tissues. *Proc Natl Acad Sci USA.* 2014;111(6):2307–2312.
18. Ganusov VV, De Boer RJ. Do most lymphocytes in humans really reside in the gut? *Trends Immunol.* 2007;28(12):514–518.
19. D'Amico R, et al. Lower CD4+ T lymphocyte nadirs may indicate limited immune reconstitution in HIV-1 infected individuals on potent antiretroviral therapy: analysis of immunophenotypic marker results of AACTG 5067. *J Clin Immunol.* 2005;25(2):106–115.
20. Acton SE, et al. Dendritic cells control fibroblastic reticular network tension and lymph node expansion. *Nature.* 2014;514(7523):498–502.
21. Skov L, et al. HuMax-CD4: a fully human monoclonal anti-CD4 antibody for the treatment of psoriasis vulgaris. *Arch Dermatol.* 2003;139(11):1433–1439.
22. Delmonico FL, et al. Nonhuman primate responses to murine and humanized OKT4A. *Transplantation.* 1993;55(4):722–728.
23. Pulito VL, et al. Humanization and molecular modeling of the anti-CD4 monoclonal antibody, OKT4A. *J Immunol.* 1996;156(8):2840–2850.
24. Padlan EA. Anatomy of the antibody molecule. *Mol Immunol.* 1994;31(3):169–217.
25. Lindmo T, Bunn PA. Determination of the true immunoreactive fraction of monoclonal antibodies after radiolabeling. *Meth Enzymol.* 1986;121:678–691.
26. Vaccari M, et al. Adjuvant-dependent innate and adaptive immune signatures of risk of SIVmac251 acquisition. *Nat Med.* 2016;22(7):762–770.
27. Hirsch V, et al. A molecularly cloned, pathogenic, neutralization-resistant simian immunodeficiency virus, SIVsmE543-3. *J Virol.* 1997;71(2):1608–1620.
28. Committee for the Update of the Guide for the Care and Use of Laboratory Animals. *Guide for the Care and Use of Laboratory Animals.* Washington DC: National Academies Press; 2011.
29. Shingai M, et al. Most rhesus macaques infected with the CCR5-tropic SHIV(AD8) generate cross-reactive antibodies that neutralize multiple HIV-1 strains. *Proc Natl Acad Sci USA.* 2012;109(48):19769–19774.
30. Cline AN, Bess JW, Piatak M, Lifson JD. Highly sensitive SIV plasma viral load assay: practical considerations, realistic performance expectations, and application to reverse engineering of vaccines for AIDS. *J Med Primatol.* 2005;34(5-6):303–312.
31. Shibata R, et al. Infection and pathogenicity of chimeric simian-human immunodeficiency viruses in macaques: determinants of high virus loads and CD4 cell killing. *J Infect Dis.* 1997;176(2):362–373.
32. Matar AJ, et al. Effect of pre-existing anti-diphtheria toxin antibodies on T cell depletion levels following diphtheria toxin-based recombinant anti-monkey CD3 immunotoxin treatment. *Transpl Immunol.* 2012;27(1):52–54.
33. Follmann D, Proschan M, Leifer E. Multiple outputation: inference for complex clustered data by averaging analyses from independent data. *Biometrics.* 2003;59(2):420–429.
34. R Core Team. R: A language and environment for statistical computing. R Foundation for Statistical Computing, Vienna, Austria. <http://www.R-project.org/>. Accessed June 4, 2018.
35. Bates DMM, Bolker B, Walker S. Fitting Linear Mixed-Effects Models Using lme4. *J Stat Softw.* 2015;67(1):1–48.
36. Kuznestova A. lmerTest: Tests in Linear Mixed Effects Models. <https://CRAN.R-project.org/package=lmerTest>. Accessed June 4, 2018.